Check for updates

International Journal of Applied Ceramic Technology

RESEARCH ARTICLE OPEN ACCESS

Processing–Property Mapping of Flash-Sintered Wall Tile Bodies

Zeynep Çetinkaya[1,2] | Yeliz Köse[3] | Betül Yıldız[3] | Ender Suvacı[4] | Rishi Raj[1]

[1]Department of Mechanical Engineering, Materials Science and Engineering, University of Colorado Boulder, Boulder, Colorado, USA | [2]Department of Metallurgical and Materials Engineering, Konya Technical University, Konya, Turkey | [3]Department of Metallurgy and Materials Engineering, Bilecik Seyh Edebali University, Bilecik, Turkey | [4]Department of Materials Science and Engineering, Eskisehir Technical University, Eskisehir, Turkey

Correspondence: Zeynep Çetinkaya (zcetinkaya@ktun.edu.tr) | Yeliz Köse (yeliz.kose@bilecik.edu.tr)

Received: 2 February 2026 | **Revised:** 11 March 2026 | **Accepted:** 30 March 2026

Keywords: energy-efficient ceramic processing | electric field-assisted sintering | flash sintering | processing-property map | wall tile ceramics

ABSTRACT

This study investigates the effects of furnace temperature (900°C and 945°C), applied electric field (50–200 V.cm^{-1}), and current density (50–150 mA.mm^{-2}) on the physical properties and microstructure of flash-sintered wall tile bodies. Water absorption, bulk density, and open porosity were measured and compared with an industrially fired reference sample. The processing–property map reveals that water absorption and density are influenced by the interaction between thermal and electrical parameters. Samples flash-sintered at 900°C satisfied the ISO 10545-3 water absorption requirement (10–20 wt%), whereas some samples processed at 945°C exhibited values below 10 wt%. Increasing furnace temperature and electric field lead to lower porosity, while higher current densities activate crystallization mechanisms and increase open porosity from 12.44% to 20.01%. These results demonstrate that simultaneous optimization of temperature, electric field, and current density is essential for tailoring wall tile properties via flash sintering (FS).

1 | Introduction

Ceramic wall tiles are widely used in the construction industry due to their desirable mechanical strength, chemical resistance, and broad decorative versatility. Performance and quality, which depend on densification, phase evolution, and final microstructure, can be regulated by the sintering mechanism [1, 2]. During the conventional firing (hereafter abbreviated as Ind) process, thermally activated mechanisms such as decomposition, polymorphic transformations, glass-phase formation, and viscous-flow sintering occur simultaneously, and as a result, mechanical strength increases while porosity decreases [1–3]. Although sintering cycles have been shortened to about 25–30 min in the ceramic tile industry [4], large-scale tile production results in high energy consumption and significant CO_2 emissions [5–9]. Although various strategies such as raw material optimization, particle size reduction, and increasing furnace efficiency have been applied to reduce the energy–carbon footprint of ceramic production, these approaches have not been able to significantly reduce the sintering temperature and time simultaneously [10, 11]. Therefore, field-assisted sintering techniques (FAST), such as spark plasma sintering (SPS), microwave sintering (MWS), and FS, which can achieve high densification rates at lower temperatures, are attracting attention [12–15].

Among these techniques, FS, introduced by Cologna et al. [16] in 2010, enables the rapid densification of the body within seconds due to the enhanced electric field applied during heating [17–19]. Compared with Ind, the ability of FS to complete the process within a few seconds and to operate at furnace temperatures several hundred degrees lower results in energy consumption that

This is an open access article under the terms of the Creative Commons Attribution License, which permits use, distribution and reproduction in any medium, provided the original work is properly cited.

© 2026 The Author(s). *International Journal of Applied Ceramic Technology* published by Wiley Periodicals LLC on behalf of American Ceramics Society.

remains below 1% of that of a conventional firing cycle [20, 21]. The main mechanisms involved in this phenomenon are local Joule heating, grain boundary overheating, and the formation of defects such as oxygen vacancies and Frenkel pairs [22–26].

FS has been successfully applied to many advanced ceramics such as BCZT [27], Al_2O_3 [28], $MgAl_2O_4$ [29], and Al_2O_3–8YSZ [30]. In addition, new methods such as touch-free flash sintering (TFFS) have been developed, which enable sintering by eliminating electrode contact through magnetic field coupling [31, 32]. Despite these advances, FS studies on materials containing glassy phases are still limited. For example, Pinter et al. [33] investigated the softening and densification behavior of soda-lime silicate glass under a DC electric field. Asymmetric ion migration caused local overheating at the anode side, demonstrating that ionic mobility is critical for the densification of the glassy phase. Prado et al. [34] showed that porous silica glass particles (95 wt% SiO_2, 2.3 wt% Na_2O, 1.6 wt% Al_2O_3) can be densified by FS under a DC electric field (1000–3000 $V.cm^{-1}$), in which the dielectric breakdown mechanism is active; they also observed that significant microstructural asymmetry occurs between the anode and cathode regions.

In addition to advanced ceramics, there are also various FS studies on conventional ceramics. Ribeiro et al. [35] showed that densification can be achieved on porcelain tiles with FS at low temperatures (~980°C–1020°C) and in a short time (30 s); however, they reported that localized glassy-phase formation can occur in the anode region due to electric field-induced softening (EFIS). They also stated that more homogeneous microstructures and higher densities can be achieved by reducing or completely eliminating the feldspar content; therefore, FS can be an energy- and time-efficient alternative to Ind. Similarly, Biesuz et al. [36] reported that porcelain tiles subjected to DC polarization can be consolidated within approximately 30 s at current densities of 4–20 $mA.mm^{-2}$ through vitrification-controlled densification, resulting in dense, homogeneous, and well-vitrified ceramics with a microstructure containing primary mullite (while secondary mullite was observed only to a limited extent).

In this study, a silicate-based industrial wall tile body composed of clay minerals, feldspar-containing components, and carbonate-bearing raw materials is investigated [1]. Such compositions contain significant amounts of alkali and alkaline earth oxides and develop a complex glass–crystalline microstructure during firing. After firing, the main crystalline phases typically include residual quartz (SiO_2), anorthite ($CaAl_2Si_2O_8$), and, depending on process conditions, gehlenite ($Ca_2Al_2SiO_7$) [1, 37]. This multiphase structure directly influences densification behavior and high-temperature electrical conductivity. Therefore, understanding the FS behavior of this industrially relevant material system is essential for evaluating its practical applicability. Our previous study [37] has shown that FS enables the densification of wall tiles in just a few seconds and at 900°C by completing the raw material reactions, thus providing significant energy and time savings. In that study, the effects of four different current densities (50, 100, 150, and 200 $mA.mm^{-2}$) were investigated under a constant electric field of 100 $V.cm^{-1}$. Higher current densities reduced water absorption of the tiles; however, the dominance of the glassy phase and the resulting immature microstructure led to lower hardness values. These findings highlight the potential of FS, but also indicate that achieving a more mature microstructure requires exploring different FS conditions and new body compositions. This need motivated further investigations into additional parameters such as electric field strength and furnace temperature.

Trombin and Raj [38] investigated the effects of current density and electric field on whiteware bodies at two different temperatures (850°C and 950°C), and demonstrated through the property map they constructed that suitable microstructures can be obtained only within a limited range of electric field values. Biesuz et al. [36] tested different electric fields to determine the onset of the flash phenomenon in their study on porcelain tiles, but did not provide a detailed evaluation of how the electric field affected the sintering behavior. Ribeiro et al. [35], on the other hand, investigated the effect of compositional variations under constant FS conditions, keeping the applied electric field fixed at 500 $V.cm^{-1}$.

Therefore, to our knowledge, the present study is the first to systematically investigate the combined effects of multiple FS parameters—applied electric field, furnace temperature, and current density—on the sintering behavior of wall tile samples. The effects of electric field (50, 100, and 200 $V.cm^{-1}$), temperature (900°C and 945°C), and current density (50, 100, and 150 $mA.mm^{-2}$) on FS behavior, phase formation, and microstructural evolution were analyzed. Furthermore, a processing-property map showing the relationship between bulk density and water absorption under different processing conditions was generated. In this respect, the study makes a significant contribution to be able to tailor microstructure and phase composition of wall tiles by controlling FS parameters precisely.

2 | Materials and Characterization

In this study, commercially available spray-dried wall tile granules were used as the starting material. The chemical composition of the commercially available spray-dried wall tile granules was determined by XRF analysis in our previous study [37]. Briefly, the composition is characterized by a silicate-rich matrix (61.47 wt.% SiO_2 and 15.18 wt.% Al_2O_3), together with moderate CaO content (5.66 wt.%) and alkali oxides ($Na_2O + K_2O \approx 4.95$ wt.%). The presence of carbonate-derived CO_2 (7.68 wt.%) indicates the contribution of carbonate-containing raw materials.

The particle size distribution of the spray-dried granules was determined by sieve analysis. The sieve apertures used in the analysis ranged from 100 to 500 μm. The results indicated that the majority of the granules were retained on the 250 and 500 μm sieves, corresponding to more than 80% of the total mass.

These granules were pressed into dogbone-shaped green samples, and the experimental setup used for the FS tests was essentially the same as that described in detail in the peer-reviewed study by Çetinkaya et al. [37] (Scheme 1). The dimensions of the green samples were 16 × 3.5 × 2 mm (length × width × thickness). To ensure the reliability and statistical validity of the study, all Ind and FS experiments were repeated three times for each set of processing parameters.

17447402, 2026, 2, Downloaded from https://ceramics.onlinelibrary.wiley.com/doi/10.1111/ijac.70178 by Turkey Cochrane Evidence Aid, Wiley Online Library on [08/04/2026]. See the Terms and Conditions (https://onlinelibrary.wiley.com/terms-and-conditions) on Wiley Online Library for rules of use; OA articles are governed by the applicable Creative Commons License

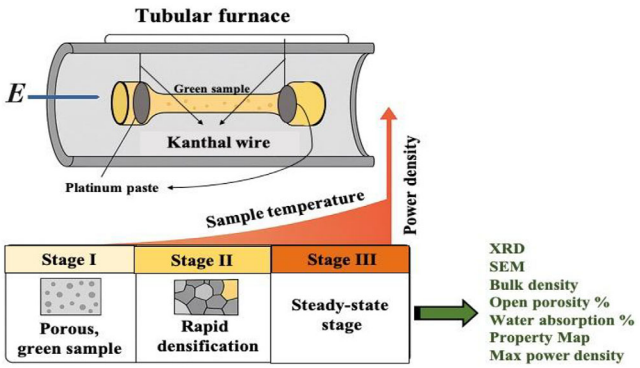

SCHEME 1 | Scheme of the FS experimental setup and model of the FS stages.

A programmable DC power supply (Glassman EW series 30 kV–66 mA, 2 kW), a data acquisition software system (Matlab), and a digital multimeter (Keithley 2000) were integrated into the setup to allow continuous monitoring of the applied electric field and current.

The furnace was heated separately for each experimental system, at a constant heating rate of 10°C.min^{-1}, to the processing temperatures of 900°C and 945°C. The furnace temperature was stabilized at the predetermined target temperature for 1 h and maintained constant (900°C or 945°C) throughout the experiment. The green samples were hooked in the center of the furnace using Kanthal wires, and a thin layer of platinum paste was applied at the contact regions between the Kanthal wires and the samples to improve electrical conductivity. The internal temperature of the samples during FS was measured using a pyrometer (Micro-Epsilon CTLM-1HCF4-C3, emissivity = 1), ensuring precise and continuous temperature control of the samples throughout the process. FS was performed under a voltage-to-current control mode at constant furnace temperature. In Stage I, a constant electric field was applied while monitoring the current response. Upon reaching the preset current density limit, the system automatically switched to current-controlled mode (Stage II), stabilizing the electrical input during the flash event. Each FS experiment lasted approximately one minute. Since a DC power supply was employed, particular attention was paid to potential microstructural gradients between the electrode regions. No visible blackening or discoloration was observed near the electrode contact areas after FS.

Due to the large number of processing parameters and samples used in the study, a coding system was developed. The coding system and explanations of parameters for all samples referenced throughout the work are shown in Scheme 2 and Table 1, respectively.

It is important to emphasize that the electric field values applied in the present study are substantially lower than those reported by Ribeiro et al. [35] (500 V.cm^{-1}) and Biesuz et al. [36] (up to 1750 V.cm^{-1} under voltage-limited conditions). However, these studies were conducted under relatively low current density limits (2–20 mA.mm^{-2}) and, in some cases, voltage-controlled regimes. In contrast, the present work employed significantly higher current density limits (50–150 mA.mm^{-2}) without pre-sintering.

The Ind process was carried out under standard production conditions, reaching a maximum temperature of 1070°C and a total firing time of 32 min [37]. The Ind and FS fired samples were analyzed to determine the effects of the different heating mechanisms on phase and microstructure development in wall tiles.

Water absorption, bulk density, and open porosity of the sintered samples were determined by Archimedes principle via the ISO 10545-3 method [31, 37, 39]. Phase analysis of sintered samples was performed using x-ray diffraction (XRD, Bruker D2 Phaser). XRD data were acquired in the 2θ range of 10° to 60° for sintered samples utilizing Cu Kα radiation (λ = 0.154 nm) at 30 kV and 10 mA, with a step size of 0.03° and a counting time of 1 s/step. (Rigaku Technologies, Inc., Nex OC+EZ). The microstructures were examined in a scanning electron microscope (SEM, Supra 40 VP, Zeiss), with an accelerating voltage of 15 kV, under high vacuum conditions, employing secondary electron imaging. The samples were polished with diamond paste and coated with a gold-palladium (Au-Pd) alloy. The central section of the sample cross-sections was analyzed for all analyses.

3 | Results and Discussion

3.1 | Processing-Property Map of the Samples

The reason for using water absorption as a parameter in the processing-property map preparation in this study is that wall tiles are defined as a product group with a water absorption value above 10% according to the international standard (ISO 10545-3). The standard also states that if the water absorption value exceeds 20%, this must be clearly stated. In this context, the study identified water absorption as a critical property that is an indicator of product performance. Figure 1 presents a processing-property map showing the changes in water absorption (%) and bulk density values of FS wall tile bodies under different conditions, along with an industrially fired sample. Therefore, in the processing-property map given in Figure 1, samples with water absorption values between 10%–20% were defined as "**Safe Area**." The water absorption values of the samples ranged from 5.92% to 14.96%, and the bulk density ranged from 1.81 to 2.13 g·cm^{-3}.

At 900°C and under an applied electric field of 100 V.cm^{-1}, increasing the current density from 50 to 150 mA.mm^{-2} results in an increase in bulk density and a decrease in water absorption. However, this trend is not maintained under an electric field of 200 V.cm^{-1}. At this electric field level, increasing the current density from 50 to 100 mA.mm^{-2} decreases water absorption, while increasing it to 150 mA.mm^{-2} causes a decrease in bulk density and subsequent increase in water absorption. Therefore, under an electric field of 200 V.cm^{-1} at 900°C, the effect of changes in current density on water absorption behavior is nonlinear.

At 945°C and 100 V.cm^{-1}, the effect of increasing current density exhibits a similar nonlinear trend. In the range of 50 → mA.mm^{-2}, bulk density increases and water absorption decreases; in the range of 100 → 150 mA.mm^{-2}, bulk density decreases, and water absorption increases again. A similar nonlinear response

17447402, 2026, 2, Downloaded from https://ceramics.onlinelibrary.wiley.com/doi/10.1111/ijac.70178 by Turkey Cochrane Evidence Aid, Wiley Online Library on [08/04/2026]. See the Terms and Conditions (https://onlinelibrary.wiley.com/terms-and-conditions) on Wiley Online Library for rules of use; OA articles are governed by the applicable Creative Commons License

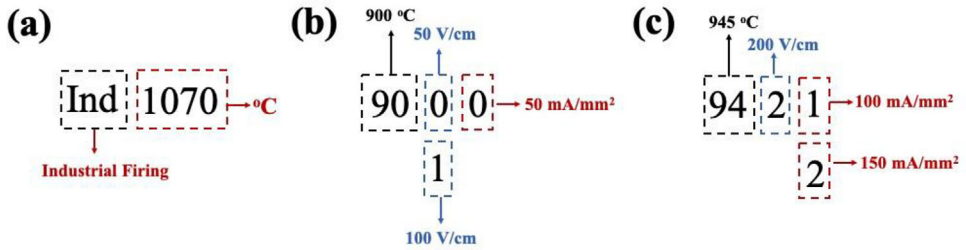

SCHEME 2 | Scheme of the (a) Ind, (b) 900°C, and (c) 945°C FS sample code system.

TABLE 1 | Parameters of Ind-FS samples.

Sample code	Furnace temperature (°C)	Electric field (V. cm^{-1})	Current density ($mA.mm^{-2}$)
Ind 1070	1070	—	—
9000	900	50	50
9010	900	100	50
9011	900	100	100
9012	900	100	150
9020	900	200	50
9021	900	200	100
9022	900	200	150
9400	945	50	50
9410	945	100	50
9411	945	100	100
9412	945	100	150
9420	945	200	50
9421	945	200	100
9422	945	200	150

is observed when 200 $V.cm^{-1}$ is applied at the same temperature. Increasing the current density from 50 to 100 $mA.mm^{-2}$ increases the bulk density, while at 150 $mA.mm^{-2}$, bulk density decreases again, and water absorption increases.

When the processing-property map is examined, it is observed that the sample (9012) FS at 900°C under a 100 $V.cm^{-1}$ electric field and a 150 $mA.mm^{-2}$ current density, and the sample (9410) FS at 945°C under a 100 $V.cm^{-1}$ electric field and a 50 $mA.mm^{-2}$ current density exhibit properties very similar to the industrially fired reference. Another observed trend detected in the processing-property is that, as the furnace temperature is increased from 900°C to 945°C, the samples sintered at 945°C generally exhibit higher bulk density and lower water absorption. When all the results are evaluated together, it is understood that the furnace temperature, the applied electric field, and the current density have a combined effect on the final physical properties.

Trombin and Raj investigated the effects of electric field and current density on ceramic whiteware bodies under two different temperatures in their FS studies [38]. They reported that although FS can be performed over a wide range of electric fields, good microstructures can be achieved only within a limited range. When the applied electric field is too low, the flash event is not triggered, or the incubation time is excessively long. Similarly, when the applied electric field is too high, the sample is damaged due to local heating. The applied electric field values in their study ranged from 500 to 3500 $V.cm^{-1}$. In this study, flash events occurred in all samples at 50, 100, and 200 $V.cm^{-1}$, and no damage was observed in any sample.

Biesuz et al. [36] also investigated the effect of current density on porcelain tiles at different temperatures. Although the effect of the electric field was not explicitly discussed in the study, the authors stated that preliminary experiments were conducted to determine the electric field range within which FS could occur. To determine the electric field required to trigger flashing at each temperature, the applied electric field was reduced in 50 $V.cm^{-1}$ steps, starting at 1750 $V.cm^{-1}$, and the minimum electric fields at which flashing occurred were determined. It was reported that the required electric field decreased as the furnace temperature increased. The electric fields determined for 900°C, 950°C, 1000°C, and 1050°C were reported as 500, 450, 400, and 350 $V.cm^{-1}$, respectively. These values were kept constant in subsequent experiments examining the effect of current density. It has also been reported that FS occurs under electric fields of 350–550 $V.cm^{-1}$ and current densities of 4–20 $mA.mm^{-2}$ at

17447402, 2026, 2, Downloaded from https://ceramics.onlinelibrary.wiley.com/doi/10.1111/ijac.70178 by Turkey Cochrane Evidence Aid, Wiley Online Library on [08/04/2026]. See the Terms and Conditions (https://onlinelibrary.wiley.com/terms-and-conditions) on Wiley Online Library for rules of use; OA articles are governed by the applicable Creative Commons License

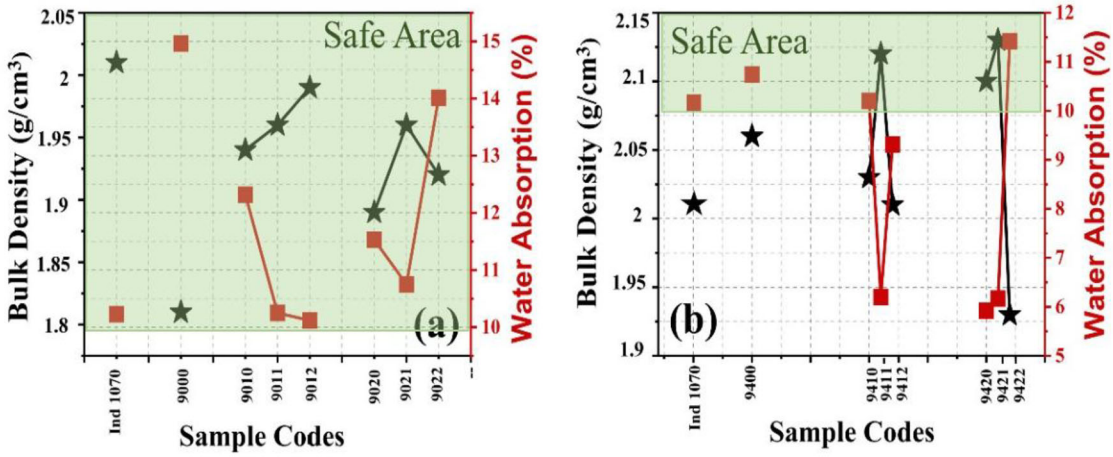

FIGURE 1 | Processing-property showing the variation of water absorption and bulk density as a function of FS conditions (a) 900°C and (b) 945°C, including the Ind sample for comparison.

TABLE 2 | Selected sample codes representing the individual effects of firing temperature, current density, and applied electric field on phase evolution and microstructural development.

Process variable investigated		Process variables held constant	Sample codes
Temperature	1070°C, 900°C, 945°C	Electric field, current density	Ind 1070, 9000, 9400
Electric field	50, 100, 200 V.cm^{-1}	Temperature, current density	9400, 9410, 9420
Current density	50, 100, 150 mA.mm^{-2}	Electric field, temperature	9420, 9421, 9422

furnace temperatures above 1000°C, and the highest bulk density and lowest open porosity are obtained at temperatures of 1050°C and above.

The increase in water absorption observed at high current densities in this study clearly parallels the behavior reported by Biesuz et al. [36] for porcelain materials. In their study, densification progressed when the current density was increased up to 14 mA.mm^{-2}, but a resurgence of swelling and open porosity was observed in the samples when the current density reached 18–20 mA.mm^{-2}. The authors attributed this behavior to the formation of irregular, large pores on the micrometer scale, observed in SEM analyses. These enlarged pores were explained by the expansion, and in some cases the opening, of the pores to the surface as a result of the buildup of internal gas pressure during the rapid softening of the glassy phase at high current density levels.

The trends detected in this processing-property map (Figure 1) indicate that densification behavior cannot be fully explained by density and water absorption alone; instead, it must be interpreted in conjunction with the underlying phase transformations and microstructural processes. Therefore, to gain a more comprehensive understanding of phase evolution, representative sample sets were selected to examine the effects of furnace temperature, current density, and applied electric field on phase and microstructure development. The selected samples are presented in Table 2. Accordingly, in the following Results sections, the XRD patterns and microstructural features of these representative samples are comparatively analyzed, providing a comprehensive assessment of the effects of field-assisted sintering parameters on phase formation and microstructural evolution.

3.2 | Phase Composition Analysis

In all XRD patterns of the study, the quartz peak at approximately $2\theta \approx 26.6°–26.9°$ exhibited the highest intensity, and was therefore used as the internal reference; the phase evolution was evaluated based on the relative changes in the other peaks with respect to this peak.

3.2.1 | Effect of Temperature on Phase Evolution

Figure 2 shows the XRD patterns of Ind 1070, 9000, and 9400 samples. A dominant quartz phase and an anorthite peak are observed in sample Ind 1070. The temperature and time being significantly different from FS allowed the reactions to complete, and the structure became stable [1].

During firing, phase formation is controlled by temperature-dependent decomposition and the subsequent reaction processes. While kaolinite decomposes into metakaolinite at approximately 490°C, the decomposition of dolomite and calcite is completed around 700°C, and this process releases CaO into the system. As a result of decomposition reactions, the formation of the high-temperature ceramic phases gehlenite and anorthite begins. Calcium carbonate plays a regulatory role in the reactions that trigger the formation of the liquid phase by decomposing into

17447402, 2026, 2, Downloaded from https://ceramics.onlinelibrary.wiley.com/doi/10.1111/ijac.70178 by Turkey Cochrane Evidence Aid, Wiley Online Library on [08/04/2026]. See the Terms and Conditions (https://onlinelibrary.wiley.com/terms-and-conditions) on Wiley Online Library for rules of use; OA articles are governed by the applicable Creative Commons License

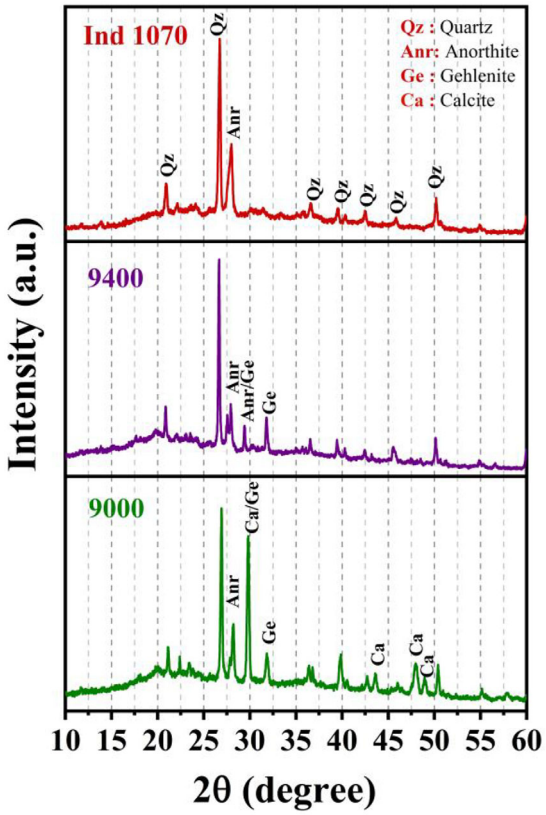

FIGURE 2 | XRD patterns of Ind 1070, 9000, and 9400 samples, illustrating the temperature-dependent phase evolution.

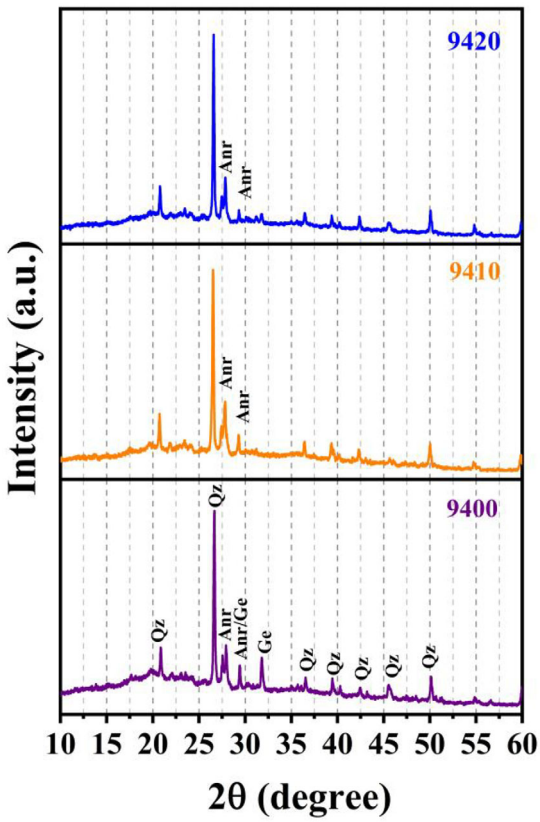

FIGURE 3 | XRD patterns of 9400, 9410, and 9420 samples, illustrating the electric field-dependent phase evolution.

CaO. At this stage, the metastable gehlenite phase forms as a result of the reaction between metakaolin and CaO; as the temperature increases, gehlenite reacts with metakaolin to transform into the thermodynamically more stable anorthite phase [3, 37]. With the progression of the reaction, free CaO is completely consumed, preventing the formation of a harmful CaO phase that could cause expansion due to moisture absorption in the structure.

Calcite peaks, positioned between 42° and 51° 2θ range, similar to those observed in the green wall tile sample [37], were detected in the sample 9000. This indicates that the decomposition reactions of calcite were not complete in that sample. This can be attributed to the too-short firing time used in FS and the low electric field and current density (50 V.cm^{-1} and 50 mA.mm^{-2}) used during sintering of the sample. In addition to quartz, the anorthite phase was also detected in all samples. The presence of anorthite suggests that some of the CaO released by the decomposition of carbonates plays a role in the formation of aluminosilicate phases [40]. Besides anorthite, gehlenite was identified in both the 9000 and 9400 specimens. In the 9000 sample, the gehlenite reflection overlaps with the calcite peak, whereas in the 9400 sample, the anorthite and gehlenite reflections exhibit intensified overlapping, suggesting that the calcite peak disappears in the 9400 sample due to the increase in temperature.

These phase analysis results are consistent with the physical properties of the samples (Figure 1). Compared to the 9000 sample, the decrease in water absorption and the increase in density observed in the 9400 sample are attributed to the disappearance of the carbonate-phase peak intensities. The Ind 1070 sample shows the lowest water absorption and highest density values, which are completely consistent with the full crystal maturation revealed in the XRD analysis [1].

3.2.2 | Effect of Electric Field on Phase Evolution

At the same temperature (945°C) and current density (50 mA.mm^{-2}), increasing the applied electric field from 50 V.cm^{-1} (9400) → 100 V.cm^{-1} (9410) → 200 V.cm^{-1} (9420) led to a systematic evolution of the crystalline phase composition and glass–crystal equilibrium in the normalized XRD patterns (Figure 3).

Increasing the electric field from 50 V.cm^{-1} (9400) to 100 V.cm^{-1} (9410) and further to 200 V.cm^{-1} (9420) led to the disappearance of the metastable gehlenite phase, suggesting a progression toward a more mature microstructural state [41]. In sample 9420, sintered at the highest electric field (200 V.cm^{-1}), the peak intensity of the anorthite phase was observed to decrease slightly. This trend in the XRD data suggests that increasing the electric field may partially suppress anorthite crystallization and promote a tendency toward more advanced microstructural maturation [42].

These phase transformations also show consistency with the density and, hence, water absorption of the specimens (Figure 1). The 9410 specimen, compared to the 9400 specimen, is associated

17447402, 2026, 2, Downloaded from https://ceramics.onlinelibrary.wiley.com/doi/10.1111/ijac.70178 by Turkey Cochrane Evidence Aid, Wiley Online Library on [08/04/2026]. See the Terms and Conditions (https://onlinelibrary.wiley.com/terms-and-conditions) on Wiley Online Library for rules of use; OA articles are governed by the applicable Creative Commons License

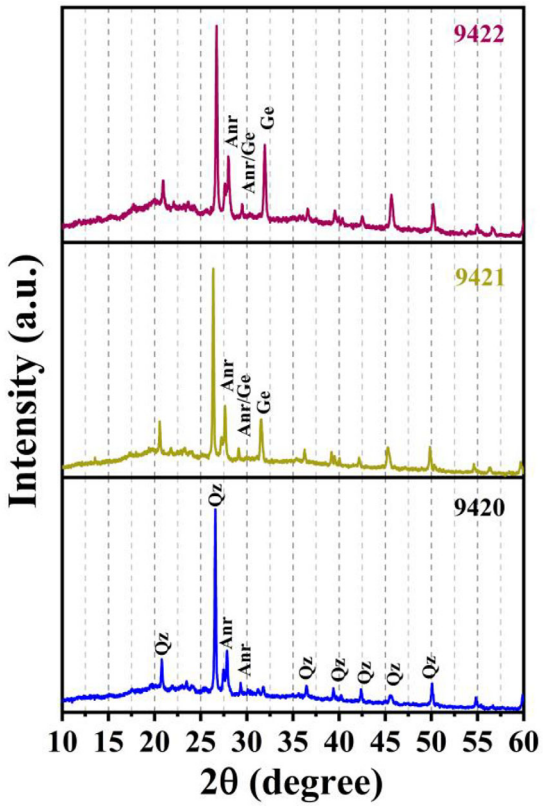

FIGURE 4 | Normalized XRD patterns of 9420, 9421, and 9422 samples, illustrating the current density-dependent phase evolution.

with a reduction in water absorption, which can be attributed to the matured structure without the gehlenite phase. Among the studied electric fields, the 9420 sample (200 V.cm^{-1}) exhibited microstructural features indicative of a more mature microstructure, accompanied by a relative reduction in anorthite peak intensity. This microstructural evolution is consistent with the observed decrease in water absorption values. The relevant result is similar to the study conducted by Biesuz et al. in the literature. In their research, Biesuz determined the onset electric field value for the relevant temperature by decreasing the electric field from 1750 V.cm^{-1} in 50 V.cm^{-1} intervals for the specified temperatures, and emphasized that the required onset value decreased with increasing temperature [36].

3.2.3 | Effect of Current Density on Phase Evolution

When the furnace temperature and electric field are kept constant (945°C, 200 V.cm^{-1}), increasing the applied current density from 50 mA.mm^{-2} (9420) → 100 mA.mm^{-2} (9421) → 150 mA.mm^{-2} (9422) leads to a systematic change in the crystalline–amorphous phase equilibrium in the normalized XRD patterns (Figure 4). Quartz appears to be the dominant phase in all samples.

In sample 9421 (100 mA.mm^{-2}), the anorthite peaks became narrower, more symmetrical, and more intense compared to sample 9420, and gehlenite formation started, indicating that crystallization progressed further [41]. In sample 9422, where the current density was increased to the maximum level (150 mA.mm^{-2}), the peaks corresponding to the gehlenite phase showed the highest sharpness and intensity, suggesting that the higher applied current strongly accelerated the crystallization process. In the 9421 and 9422 specimens, the anorthite and gehlenite peaks exhibit noticeable overlap. In contrast, an increase in the amorphous contribution indicates that crystalline and non-crystalline regions coexist, and the sample exhibits a more mixed-phase character [36].

When the phase evolution driven by increasing current density is evaluated together with the measured water absorption values (Figure 1), a different trend emerges. The relatively low water absorption value in 9420 is consistent with a limited but more homogeneous crystalline–amorphous phase equilibrium [43]. In 9421, despite the increase in crystalline order, there was no decrease in water absorption values; on the contrary, a slight increase was observed. Similarly, the further enhancement of anorthite and gehlenite peaks in specimen 9422 suggests that excessive crystalline phase development competes with the formation and redistribution of the glassy phase, limiting its continuity and fluidity, thus weakening the densification mechanisms during FS. Therefore, the pores may not close effectively, and water absorption increases even though the degree of crystallization is higher.

3.3 | Microstructure Evolution

SEM images of wall tile bodies, FS under different conditions, and those fired in an industrial environment are shown in Figure 5. The presented SEM micrographs primarily aim to illustrate the post-firing microstructural maturation of the body and the general distribution of open porosity. The irregular morphology of the pores, together with the presence of sharp-edged quartz grains, is characteristic of a limited extent of liquid-phase sintering [44]. Based on combined XRD analysis and typical microstructural features of wall tile bodies, the relatively dark and coarse grains are attributed to residual quartz particles. To support microstructural interpretation, the experimentally determined open porosity percentages of the specimens are shown in Figure 6. The relevant values are written in yellow over the microstructure photographs in Figure 5. As seen in Figure 6a, the specimen FS at 945°C exhibited lower porosity than the specimen FS at 900°C, while Ind 1070 fired at 1070°C exhibited the lowest porosity. An increasing electric field caused a decrease in porosity, similar to increasing temperature (Figure 6b). However, increasing current density caused an increase in porosity (Figure 6c).

The effect of sintering temperature on the microstructure during FS is shown in comparison with the industrial product in Figure 5a–c. When the microstructures are examined, it is observed that the structure acquires a more mature structure with increasing FS temperature. The most mature microstructure is observed in the Ind 1070 specimen. This observation is consistent with the decrease in porosity. The highest porosity value was determined as 27.01% in the 9000 specimen, while the corresponding value was determined as 20.61% in the Ind 1070 specimen. When the obtained microstructures are evaluated together with the XRD results, it is observed that the calcite phase is still dominant in the 9000 specimen after FS processing. The presence of this carbonate phase supports the immature structure seen in the SEM images.

17447402, 2026, 2, Downloaded from https://ceramics.onlinelibrary.wiley.com/doi/10.1111/ijac.70178 by Turkey Cochrane Evidence Aid, Wiley Online Library on [08/04/2026]. See the Terms and Conditions (https://onlinelibrary.wiley.com/terms-and-conditions) on Wiley Online Library for rules of use; OA articles are governed by the applicable Creative Commons License

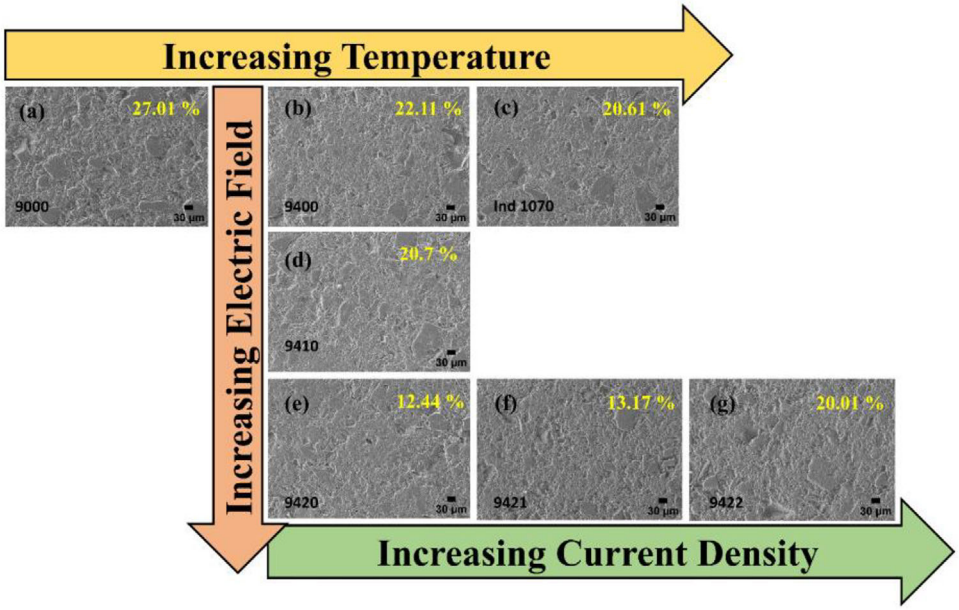

FIGURE 5 | Combined influence of increasing temperature (a)–(c), electric field (b), (d), and (e), and current density (e)–(g) on the microstructural development and open porosity (%) of FS and Ind wall tile specimens.

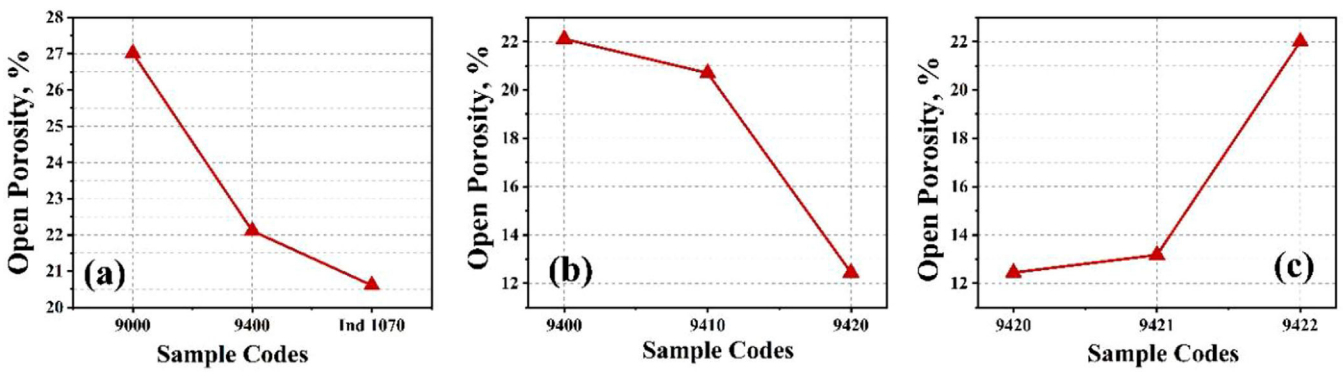

FIGURE 6 | Open porosity (%) values of the wall tile bodies under different (a) temperature, (b) electric field, and (c) current density conditions.

The effect of the electric field on the microstructure during FS is given in Figure 5b,d,e. Increasing the electric field from 50 to 100 and 150 V.cm^{-1} produced an effect similar to that of temperature. A more mature microstructure is achieved in the specimens with increasing voltage. The decrease in porosity supported this observation. While the specimen FS at 50 V.cm^{-1} exhibited 22.11% open porosity, increasing the electric field to 200 V.cm^{-1}, the porosity value decreased to 12.44%. As the electric field was increased from 50 to 100 and 200 V.cm^{-1}, the gehlenite phase disappeared. This phase transformation in XRD is consistent with the transition to a more mature microstructure observed in SEM images.

The effect of increasing current density during FS on the microstructure is given in Figure 5e–g. As the current density increased from 50 to 150 mA.mm^{-2}, the structure became less mature. When the current density was 50 mA.mm^{-2}, the open porosity was 12.44%, whereas increasing the current density to 150 mA.mm^{-2} raised the porosity to 20.01%. Similarly, the bulk density in the relevant specimens exhibited a decreasing trend, as expected. With an increase in the current value from 50 to 150 mA.mm^{-2}, the bulk density decreased from 2.10 to 1.93 g.cm^{-3} (Figure 1). When the XRD patterns of the relevant specimens are examined, it is seen that the increasing current density promotes gehlenite crystallization again in addition to anorthite crystallization. The increasing crystalline content suggests that some of the glassy phase may have been consumed during crystallization, or the crystal structure may have acted as a rigid skeleton restricting the fluidity of the remaining glassy phase. In either case, pore closure becomes more difficult.

Biesuz et al. [36] reported that increasing current density reduces porosity in the structure up to a certain level, but above a certain current density, the pores swell, causing the sample to expand macroscopically. They attributed the increased porosity to increased glassy phase development. In the current study, higher current densities increased crystallization intensity rather than increasing the glassy phase content;

17447402, 2026, 2, Downloaded from https://ceramics.onlinelibrary.wiley.com/doi/10.1111/ijac.70178 by Turkey Cochrane Evidence Aid, Wiley Online Library on [08/04/2026]. See the Terms and Conditions (https://onlinelibrary.wiley.com/terms-and-conditions) on Wiley Online Library for rules of use; OA articles are governed by the applicable Creative Commons License

the increased tendency for crystallization resulted in higher porosity.

Although phase evolution influences densification behavior, water absorption is primarily governed by open porosity in accordance with ISO 10545-3. The phase composition affects water absorption indirectly through its control over microstructural development and pore closure mechanisms. For instance, increased glass phase continuity enhances viscous flow and reduces open porosity, thereby lowering water absorption. Conversely, excessive crystallization may hinder effective pore closure and lead to higher open porosity, resulting in increased water absorption. Therefore, porosity is the direct controlling parameter, while phase composition acts as an indirect microstructural regulator.

3.4 | Relationship Between Power Density and Microstructure Evolution in Flash Sintering

The FS process can be examined in three main stages: (1) the initial period under voltage control, where the material does not exhibit high electrical conductivity; (2) the transition period, where the conductivity increases rapidly; and (3) the final period, where the experiment proceeds stably under current-controlled conditions.

In this study, unlike the previous study [37], it was determined that the FS behavior of wall tile depends on the changes in the applied electric field (50–200 $V.cm^{-1}$), current density (50–150 $mA.mm^{-2}$), and furnace temperature (900°C and 945°C). As the furnace temperature increases, the electric field values selected for FS can be reduced, thus determining the sintering parameters of the specimens. The interaction of thermal energy and the applied electric field (Stage I) led to a rapid densification that occurs within only a few seconds, which is significantly different from the gradual densification observed in conventional sintering. In Stage II, a significant increase in current was observed at the moment FS occurs. This behavior is consistent with the results widely reported in the literature for oxide-based ceramics [16, 19, 25, 31, 36, 37], confirming the current increase in response of the system. As a result, it was concluded that maintaining the delicate balance between furnace temperature and electric field/current density is of critical importance to achieve stable and controlled instantaneous sintering of wall tile bodies.

Although these three stages were described in detail in a previous study [37], the internal temperatures of each specimen, particularly during Stage III, are explicitly reported in this study (Figure 7). Figure 7 also shows the relationship between the power density and current density limits for each furnace temperature and composition. In all experiments, the applied electric fields in Stage I were held constant at 50, 100, and 200 $V.cm^{-1}$; in Stage II, the applied current densities were set in the range of 50–150 $mA.mm^{-2}$. Due to Joule heating resulting from the applied current, specimen temperatures were reported to slightly exceed the furnace temperature.

During the initial phase, the electrical conductivity of the ceramic material gradually increases, and the specific power density

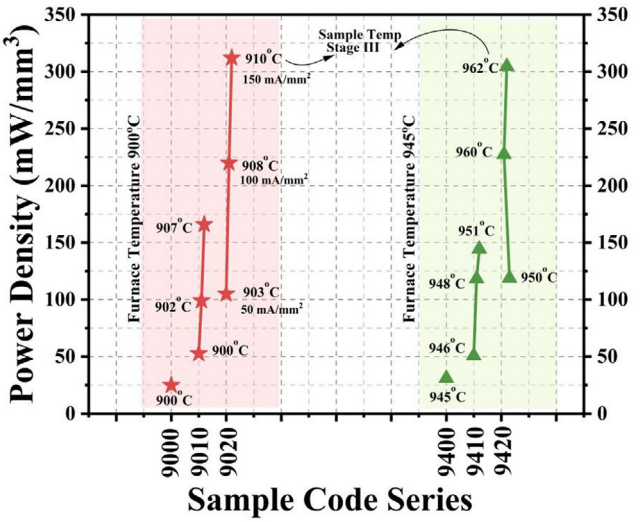

FIGURE 7 | Maximum power density of FS wall tile samples processed under different electric fields and current densities at furnace temperatures of 900°C (red) and 945°C (green). Inner temperature data points represent the specimen temperatures measured at Stage III of the flash.

increases accordingly (Stage I). This phase results in sudden sintering, characterized by sharp power peaks (maximum power density) and a sudden drop in electrical resistance, as seen in Figure 7. Immediately following this sudden increase, the power supply switches to current-controlled mode (Stage II) to stabilize the electrical power input. This time, which represents the transition from the insulating to the conducting state, is highly sensitive to the magnitude of the applied electric field. The incubation time was defined as the duration between the application of the external electric field and the sudden rise in current associated with the flash event. This parameter was found to decrease with increasing furnace temperature and applied electric field. Specimens exposed to higher electric fields exhibited significantly shorter incubation times; this trend is consistent with behavior observed in other crystalline ceramic systems.

Analysis of the power density distribution obtained from wall tile specimens provides critical information about the densification, phase formation, and microstructural evolution that occur during the FS process. When these data are evaluated together with bulk density, water absorption, porosity measurements, and SEM/XRD observations, significant correlations emerge. Specimens from the 900°C series exhibited significantly lower power densities of 24.7 $mW.mm^{-3}$ at 50 $V.cm^{-1}$, 50–150 $mW.mm^{-3}$ at 100 $V.cm^{-1}$ [37], and 52–166 $mW.mm^{-3}$ at 200 $V.cm^{-1}$. At 945°C, specimens subjected to an electrical load of 200 $V.cm^{-1}$ reached power densities in the range of approximately 119–332 $mW.mm^{-3}$, with 30.96 $mW.mm^{-3}$ at 50 $V.cm^{-1}$ and 50.7–144.38 $mW.mm^{-3}$ at 100 $V.cm^{-1}$. These conditions were associated with the highest densities, lowest water absorption, and most enhanced microstructural compaction across all characterization results. This also suggests that higher power dissipation increases densification and/or crystallization density. Conversely, in the FS specimens processed at 900°C furnace temperatures, higher porosity, partially preserved granular structure, and insufficient

17447402, 2026, 2, Downloaded from https://ceramics.onlinelibrary.wiley.com/doi/10.1111/ijac.70178 by Turkey Cochrane Evidence Aid, Wiley Online Library on [08/04/2026]. See the Terms and Conditions (https://onlinelibrary.wiley.com/terms-and-conditions) on Wiley Online Library for rules of use; OA articles are governed by the applicable Creative Commons License

power density limit thermal runaway, thus reducing FS effectiveness.

Although both temperature series reached similar maximum power levels, specimens sintered at 945°C reached these values with lower current and voltage inputs. This can be explained by increased matrix conductivity and a lower initial electric field requirement. Therefore, matching a low electric field and optimal furnace temperature can increase the energy efficiency of the FS process. Increasing furnace temperature and electric field resulted in an increase in power density, resulting in the formation of more mature microstructures. However, while increasing current density at constant temperature and electric field increased power density, it also promoted crystallization and restricted densification (leading to an increase in the amount of open porosity), resulting in less mature structures. The significant divergence between the 900°C and 945°C groups highlights the critical role of furnace temperature, particularly for industrial wall tile applications. In summary, this comprehensive analysis demonstrates that rapid densification and improved microstructural integrity are strongly dependent on achieving adequate power dissipation, highlighting furnace temperature as a key parameter for energy-efficient and industrially applicable FS conditions.

4 | Conclusions

In this study, how the microstructural and physical properties of wall tile bodies change as a function of FS parameters (temperature, current density, electric field) was systematically investigated.

The "Safe Area" in the processing-property map was created to achieve the acceptable water absorption values specified in the ISO 10545-3 standard. It was observed that the Ind 1070 sample (10.23%), all samples in the 9000 series, and samples coded 9410–9422 in the 9400 series were located in the "Safe Area." It was observed that the flash parameters had a synergistic interaction in determining the physical properties of the samples. In order to determine these synergistic effects, each parameter in the flash parameters was examined by keeping the other parameters constant, and sample sets were created accordingly: I. temperature effect (Ind 1070, 9000, 9400), II. electric field effect (9400, 9410, 9420), III. current density effect (9420, 9421, 9422).

The Ind 1070 specimen fired at 1070°C exhibited a stable structure containing only anorthite and quartz phases. Considering the phase development and the decrease in porosity, it was observed that the temperature increases in the FS mechanism resulted in a more mature microstructure. The fact that only samples 9410 and 9422 of the 9400 series were found in the safe area indicates that temperature is not the only effective parameter in determining the safe area boundaries. Increasing the electric field caused physical and microstructural changes similar to those observed with increasing temperature. In particular, for sample 9420, the maximum electric field and the significant reduction in open porosity lowered the water absorption value to 5.92%, pushing it outside the safe region. Therefore, according to the processing-property map, the optimum electric field at 945°C can be identified as 100 $V.cm^{-1}$. In the 942* series, although increasing the current density from 50 to 150 $mA.mm^{-2}$ (*) promotes crystallization, it does not lead to the expected improvement in densification. At the highest current density (9422), the re-emergence of metastable gehlenite phases and the excessively accelerated crystalline phase formation compete with the development and redistribution of the glassy phase, thereby preventing effective closure of open pores and resulting in an unexpected increase in water absorption (11.42%). This information indicates that a specific current density should be carefully considered when FS of wall tile bodies. While the study focused on % water absorption, % open porosity, and bulk density for wall tiles, another crucial factor for wall tiles is their strength.

The internal specimen temperature data confirms that Joule heating plays a decisive role in sustaining the flash regime. These power densities and internal temperatures, together with the other analyses, confirm that the transformation reactions of the raw material components into the final phases were successfully completed in all series, except for the 9000 specimen, in which the temperature, applied voltage, and current density were the lowest.

This study systematically demonstrated for the first time the critical power density ranges, optimum electrical conditions [synergistic effects], phase development→microstructure→physical property linkage in FS of wall tile bodies, and also showed the potential for significant reduction in energy consumption by reducing the sintering temperature and time.

Future work will focus on scaling the proposed FS approach to full-size ceramic tiles by optimizing electric field distribution and electrode configurations suitable for large-area geometries. Particular attention will be given to the development of touch-free electrode systems capable of producing uniform electrical fields across flat tile surfaces. Based on this study's results will be essential for translating laboratory-scale FS results into practical industrial firing technologies for ceramic tile manufacturing.

Author Contributions

Zeynep Çetinkaya: writing – original draft, data curation, formal analysis, conceptualization, methodology, visualization, review and editing. **Yeliz Köse:** writing – original draft, data curation, formal analysis, conceptualization, methodology, visualization, review and editing. **Betül Yıldız:** writing – original draft, data curation, formal analysis, conceptualization, methodology, visualization, review and editing. **Ender Suvacı:** conceptualization, methodology, review and editing. **Rishi Raj:** conceptualization, methodology, review and editing.

Acknowledgments

Zeynep Çetinkaya thanks TUBITAK 2219–International Postdoctoral Research Fellowship Program for supporting her research at the University of Colorado at Boulder. All authors thank the Veli Akgün Ceramic Factory, Eskişehir, Türkiye, for the materials support.

Conflicts of Interest

The authors declare no conflicts of interest.

17447402, 2026, 2, Downloaded from https://ceramics.onlinelibrary.wiley.com/doi/10.1111/ijac.70178 by Turkey Cochrane Evidence Aid, Wiley Online Library on [08/04/2026]. See the Terms and Conditions (https://onlinelibrary.wiley.com/terms-and-conditions) on Wiley Online Library for rules of use; OA articles are governed by the applicable Creative Commons License

Data Availability Statement

The data that support the findings of this study are available from the corresponding author upon reasonable request.

References

1. J. G. S. Sidnei and N. F. Jose, "Sintering Behavior of Porous Wall Tile Bodies During Fast Single-Firing Process," *Materials Research* 8, no. 2 (2005): 197–200, https://doi.org/10.1590/S1516-14392005000200020.

2. O. Cengiz and A. Kara, "Effect of Alkaline-Earth Oxides on Firing Behaviour of Monoporosa Wall Tile Bodies," *Journal of Ceramic Processing Research* 19, no. 3 (2018): 189–197, https://doi.org/10.36410/jcpr.2018.19.3.189.

3. S. J. G. Sousa and J. N. F. Holanda, "Thermal Transformations of Red Wall Tile Pastes," *Journal of Thermal Analysis and Calorimetry* 87 (2007): 423–428, https://doi.org/10.1007/s10973-006-7030-7.

4. R. Elias, A. Zaccaron, O. R. K. Montedo, et al., "Pyroplastic Deformation Analysis of Brazilian Porcelain Tile Formulations Using Mixture Design," *International Journal of Applied Ceramic Technology* 21 (2024): 4241–4256, https://doi.org/10.1111/ijac.14813.

5. H. Jouhara, D. Bertrand, B. Axcell, et al., "Investigation on a Full-Scale Heat Pipe Heat Exchanger in the Ceramics Industry for Waste Heat Recovery," *Energy* 223 (2021): 120037, https://doi.org/10.1016/j.energy.2021.120037.

6. C. Agrafiotis and T. Tsoutsos, "Energy Saving Technologies in the European Ceramic Sector: A Systematic Review," *Applied Thermal Engineering* 21, no. 12 (2001): 1231–1249, https://doi.org/10.1016/S1359-4311(01)00006-0.

7. I. González, E. Galán, A. Miras, and M. Vázquez, "CO_2 Emissions Derived From Raw Materials Used in Brick Factories: Applications to Andalusia (Southern Spain)," *Applied Clay Science* 52 (2011): 193–198, https://doi.org/10.1016/j.clay.2011.01.003.

8. D. D. F. Del Rio, B. K. Sovacool, A. M. Foley, et al., "Decarbonizing the Ceramics Industry: A Systematic and Critical Review of Policy Options, Developments and Sociotechnical Systems," *Renewable Sustainable Energy Reviews* 157 (2022): 112081, https://doi.org/10.1016/j.rser.2022.112081.

9. D. Gabaldón-Estevan, A. Mezquita, S. Ferrer, and E. Monfort, "Unwanted Effects of European Union Environmental Policy to Promote a Post-Carbon Industry: The Case of Energy in the European Ceramic Tile Sector," *Journal of Cleaner Production* 117 (2016): 41–49, https://doi.org/10.1016/j.jclepro.2016.01.021.

10. G. Han, N. Zheng, and J. Wu, "Function Optimization of Ceramic Firing Process and Reduction of Energy Consumption Based on CFD Simulation," *Journal of Physics: Conference Series* 1 (2024): 012003, https://doi.org/10.1088/1742-6596/2729/1/012003.

11. C. L. Alves, V. Skorych, A. De Noni, et al., "Improving the Sustainability of Porcelain Tile Manufacture by Flowsheet Simulation," *Ceramics International* 49, no. 14B (2023): 24581–24597, https://doi.org/10.1016/j.ceramint.2023.01.056.

12. R. W. Harrison, J. Morgan, J. Buckley, et al., "Development and Comparison of Field Assisted Sintering Techniques to Densify CeO_2 Ceramics," *Journal of the European Ceramic Society* 42, no. 14 (2022): 6599–6607, https://doi.org/10.1016/j.jeurceramsoc.2022.06.079.

13. Y. Li, L. Zhang, K. Kisslinger, and Y. Wu, "Field-Assisted Sintering and Phase Transition of ZnS–$CaLa_2S_4$ Composite Ceramics," *Journal of the European Ceramic Society* 37, no. 15 (2017): 4741–4749, https://doi.org/10.1016/j.jeurceramsoc.2017.07.009.

14. E. Śnieżek, J. Szczerba, P. Stoch, et al., "Structural Properties of MgO–ZrO_2 Ceramics Obtained by Conventional Sintering, Arc Melting and Field Assisted Sintering Technique," *Materials and Design* 99 (2016): 412–420, https://doi.org/10.1016/j.matdes.2016.03.106.

15. F. Chen, D. Jin, K. Tyeb, et al., "Field Assisted Sintering of Graphene Reinforced Zirconia Ceramics," *Ceramics International* 41, no. 4 (2015): 6113–6116, https://doi.org/10.1016/j.ceramint.2014.12.147.

16. M. Cologna, B. Rashkova, and R. Raj, "Flash Sintering of Nanograin Zirconia in <5 s at 850°C," *Journal of the American Ceramic Society* 93, no. 11 (2010): 3556–3559, https://doi.org/10.1111/j.1551-2916.2010.04089.x.

17. V. M. Sglavo, E. D. Bona, and I. Mazo, "Flash Sintering of Metal-Like Ceramics: A Short Overview," *Ceramics International* 50, no. 19C (2024): 37356–37365, https://doi.org/10.1016/j.ceramint.2024.05.018.

18. T. P. Mishra, V. Avila, R. R. I. Neto, M. Bram, O. Guillon, and R. Raj, "On the Role of Debye Temperature in the Onset of Flash in Three Oxides," *Scripta Mater* 170 (2019): 81–84, https://doi.org/10.1016/j.scriptamat.2019.05.030.

19. D. Yadav and R. Raj, "Two Unique Measurements Related to Flash Experiments With Yttria-Stabilized Zirconia," *Journal of the American Ceramic Society* 100 (2017): 5374–5378, https://doi.org/10.1111/jace.15114.

20. S. Grasso, Y. Sakka, N. Rendtorff, et al., "Modeling of the Temperature Distribution of Flash Sintered Zirconia," *Journal of the Ceramic Society of Japan* 119 (2011): 144–146, https://doi.org/10.2109/jcersj2.119.144.

21. J. G. P. Da Silva, H. A. Al-Qureshi, F. Keil, and R. Janssen, "A Dynamic Bifurcation Criterion for Thermal Runaway During the Flash Sintering of Ceramics," *Journal of the European Ceramic Society* 36 (2016): 1261–1267, https://doi.org/10.1016/j.jeurceramsoc.2015.11.048.

22. R. Chaim and C. Estournès, "On Thermal Runaway and Local Endothermic/Exothermic Reactions During Flash Sintering of Ceramic Nanoparticles," *Journal of Materials Science* 53 (2018): 6378–6389, https://doi.org/10.1007/s10853-018-2040-y.

23. J. Narayan, "A New Mechanism for Field-Assisted Processing and Flash Sintering of Materials," *Scripta Materialia* 69 (2013): 107–111, https://doi.org/10.1016/j.scriptamat.2013.02.020.

24. H. Yoshida, "Control of High Temperature Mass Transport Phenomena Through Grain Boundaries in Oxide Ceramics Based on Grain Boundary Chemical Composition and External Electric Field," *Journal of the Ceramic Society of Japan* 130 (2022): 762–769, https://doi.org/10.2109/jcersj2.22070.

25. R. Raj, M. Cologna, and J. S. C. Francis, "Influence of Externally Imposed and Internally Generated Electrical Fields on Grain Growth, Diffusional Creep, Sintering and Related Phenomena in Ceramics," *Journal of the American Ceramic Society* 94 (2011): 1941–1965, https://doi.org/10.1111/j.1551-2916.2011.04652.x.

26. M. Jongmanns, R. Raj, and D. E. Wolf, "Generation of Frenkel Defects Above the Debye Temperature by Proliferation of Phonons Near the Brillouin Zone Edge," *New Journal of Physics* 20 (2018): 093013, https://doi.org/10.1088/1367-2630/aadd5a.

27. A. Taibi, E. G. González, B. Yang, et al., "Step-Wise Current Reactive Flash Sintering of $Ba_{0.85}Ca_{0.15}Ti_{0.90}Zr_{0.10}O_3$ (BCZT) Ceramics: Structure and Electrical Properties," *Journal of the European Ceramic Society* 46 (2025): 117845, https://doi.org/10.1016/j.jeurceramsoc.2025.117845.

28. S. Kong, R. Pang, Y. Dai, et al., "Enhancing the Microstructure of DC Flash-Sintered High-Purity Al_2O_3 Ceramics by Stepwise Increase in Current Density," *Ceramics International* 51, no. 19B (2025): 28912–28918, https://doi.org/10.1016/j.ceramint.2025.04.101.

29. N. Han, S. Yang, S. Chen, et al., "Effects of Limiting Current Density and Current Step Rate on Microstructure and Hardness of Flash Sintered $MgAl_2O_4$ Ceramics," *Journal of the European Ceramic Society* 45, no. 3 (2025): 116982, https://doi.org/10.1016/j.jeurceramsoc.2024.116982.

30. S. Yao, Y. Liu, D. Liu, K. Zhao, and J. Liu, "Effect of the Al_2O_3 Content on the Microstructure Evolution of Flash-Sintered Al_2O_3–8YSZ Ceramics," *Open Ceramics* 16 (2023): 100468, https://doi.org/10.1016/j.oceram.2023.100468.

31. Z. Çetinkaya and R. Raj, "Processing Map for Touch-Free Flash Sintering of a Whiteware Ceramic," *Journal of the American Ceramic Society* 107 (2024): 5720–5727, https://doi.org/10.1111/jace.19875.

17447402, 2026, 2, Downloaded from https://ceramics.onlinelibrary.wiley.com/doi/10.1111/ijac.70178 by Turkey Cochrane Evidence Aid, Wiley Online Library on [08/04/2026]. See the Terms and Conditions (https://onlinelibrary.wiley.com/terms-and-conditions) on Wiley Online Library for rules of use; OA articles are governed by the applicable Creative Commons License

32. S. I. A. Jalali and R. Raj, "Touch-Free Flash Sintering With Magnetic Induction Within a Reactor Activated by the Usual Flash Method," *Journal of the American Ceramic Society* 105, no. 11 (2022): 6517–6522, https://doi.org/10.1111/jace.18601.

33. L. Pinter, M. Biesuz, V. M. Sglavo, et al., "DC-Electro Softening in Soda Lime Silicate Glass: An Electro-Thermal Analysis," *Scripta Materialia* 151 (2018): 14–18, https://doi.org/10.1016/j.scriptamat.2018.03.028.

34. M. O. Prado, M. Biesuz, M. Frasnelli, F. E. Benedetto, and V. M. Sglavo, "Viscous Flow Flash Sintering of Porous Silica Glass," *Journal of Non-Crystalline Solids* 476 (2017): 60–66, https://doi.org/10.1016/j.jnoncrysol.2017.09.024.

35. C. Ribeiro, L. Figueiredo, R. Serrazina, et al., "Flash Sintering of Porcelain Stoneware: Effect of Composition Modifications," *Journal of the European Ceramic Society* 43, no. 9 (2023): 4189–4197, https://doi.org/10.1016/j.jeurceramsoc.2023.03.008.

36. M. Biesuz, W. D. Abate, and V. M. Sglavo, "Porcelain Stoneware Consolidation by Flash Sintering," *Journal of the American Ceramic Society* 101 (2018): 71–81, https://doi.org/10.1111/jace.15162.

37. Z. Çetinkaya, B. Yıldız, Y. Köse, E. Suvacı, and R. Raj, "Comparison of Flash Sintering and Industrial Firing of Ceramic Wall Tiles: Microstructure and Properties," *International Journal of Applied Ceramic Technology* 23 (2025): e70089, https://doi.org/10.1111/ijac.70089.

38. F. Trombin and R. Raj, "Developing Processing Maps for Implementing Flash Sintering Into Manufacture of Whiteware Ceramics," *American Ceramic Society Bulletin* 93 (2014): 32–35.

39. E. Suvacı and N. Tamsu, "The Role of Viscosity on Microstructure Development and Stain Resistance in Porcelain Stoneware Tiles," *Journal of the European Ceramic Society* 30 (2010): 3071–3077, https://doi.org/10.1016/j.jeurceramsoc.2010.06.010.

40. S. Ke, X. Cheng, Y. Wang, Q. Wang, and H. Wang, "Dolomite, Wollastonite and Calcite as Different CaO Sources in Anorthite-Based Porcelain," *Ceramics International* 39 (2013): 4953–4960, https://doi.org/10.1016/j.ceramint.2012.11.091.

41. K. Traoré, T. S. Kabré, and P. Blanchart, "Gehlenite and Anorthite Crystallisation From Kaolinite and Calcite Mix," *Ceramics International* 29, no. 4 (2003): 377–383, https://doi.org/10.1016/S0272-8842(02)00148-7.

42. M. Biesuz and V. M. Sglavo, "Flash Sintering of Ceramics," *Journal of the European Ceramic Society* 39 (2019): 115–143, https://doi.org/10.1016/j.jeurceramsoc.2018.08.048.

43. Z. B. Ozturk and N. Ay, "Investigation of Porosity of Ceramic Tiles by Means of Image Analysis Method," *Journal of Ceramic Processing Research* 15, no. 6 (2014): 393–397, https://doi.org/10.36410/jcpr.2014.15.6.393.

44. J. L. Amorós, M. J. Orts, S. Mestre, J. Garcia-Ten, and C. Feliu, "Porous Single-Fired Wall Tile Bodies: Influence of Quartz Particle Size on Tile Properties," *Journal of the European Ceramic Society* 30 (2010): 17–28, https://doi.org/10.1016/j.jeurceramsoc.2009.08.001.

17447402, 2026, 2, Downloaded from https://ceramics.onlinelibrary.wiley.com/doi/10.1111/ijac.70178 by Turkey Cochrane Evidence Aid, Wiley Online Library on [08/04/2026]. See the Terms and Conditions (https://onlinelibrary.wiley.com/terms-and-conditions) on Wiley Online Library for rules of use; OA articles are governed by the applicable Creative Commons License